Journal of Nuclear Medicine, published on February 28, 2020 as doi:10.2967/jnumed.119.239343

High Resolution Depth-Encoding PET Detector Module with Prismatoid Light Guide Array

Andy LaBella[1*], Xinjie Cao[2], Eric Petersen[1], Rick Lubinsky[3], Anat Biegon[3], Wei Zhao[3] & Amir H. Goldan[3**]

[1]Department of Biomedical Engineering, College of Engineering and Applied Sciences, Stony Brook University, Stony Brook, NY, US
[2]Department of Electrical and Computer Engineering, College of Engineering and Applied Sciences, Stony Brook University, Stony Brook, NY, US
[3]Department of Radiology, Renaissance School of Medicine, Stony Brook University, Stony Brook, NY, US

[*]101 Nicolls Road, Stony Brook, NY, 11794
Phone: (914) 380-2785
Fax: (631) 444-7538
Email: Andrew.LaBella@stonybrook.edu
[**]101 Nicolls Road, Stony Brook, NY, 11794
Phone: (631) 638-8537
Fax: (631) 444-7538
Email: Amirhossein.Goldan@stonybrookmedicine.edu

Word Count: 4427

Running Title: Prism-PET: TOF-DOI-Compton PET

ABSTRACT

Depth-encoding detectors with single-ended readout provide a practical, cost-effective approach for constructing high resolution and high sensitivity PET scanners. However, the current iteration of such detectors utilizes a uniform glass light guide to achieve depth-encoding, resulting in non-uniform performance throughout the detector array due to suboptimal intercrystal light sharing. We introduce Prism-PET, a single-ended readout PET detector module with a segmented light guide composed of an array of prismatoids that introduces enhanced, deterministic light sharing. **Methods:** High resolution PET detector modules were fabricated with single-ended readout of polished multicrystal lutetium yttrium orthosilicate (LYSO) scintillator arrays directly coupled 4-to-1 and 9-to-1 to arrays of 3.2 × 3.2 mm^2 silicon photomultiplier pixels. Each scintillator array was coupled at the non-readout side to a light guide (one 4-to-1 module with a uniform glass light guide, one 4-to-1 Prism-PET module and one 9-to-1 Prism-PET module) to introduce intercrystal light sharing, which closely mimics the behavior of dual-ended readout with the additional benefit of improved crystal identification. Flood histogram data was acquired using a 3 MBq Na-22 source to characterize crystal identification and energy resolution. Lead collimation was used to acquire data at specific depths to determine depth-of-interaction (DOI) resolution. **Results:** The flood histogram measurements showed excellent and uniform crystal separation throughout the Prism-PET modules while the uniform glass light guide module had performance degradation at the edges and corners. A DOI resolution of 5.0 mm full width at half maximum (FWHM) and energy resolution of 13% were obtained in the uniform glass light guide module. By comparison, the 4-to-1 coupled Prism-PET module achieved 2.5 mm FWHM DOI resolution and 9% energy resolution. **Conclusions:** PET scanners based on our Prism-PET modules with segmented prismatoid light guide arrays can achieve high and uniform spatial resolution (9-to-1 coupling with ~ 1 mm crystals), high sensitivity, good energy and timing resolutions (using polished crystals and after applying DOI-correction), and compact size (depth-encoding eliminates parallax error and permits smaller ring-diameter).

INTRODUCTION

Molecular imaging with PET is a powerful technique used primarily for diagnosis, treatment selection, treatment monitoring and research in cancer (*1*) and neuropsychiatric disorders (*2*). Despite its high molecular specificity, quantitative nature and clinical availability, PET has not been able to achieve its full potential as the go-to molecular imaging modality due in large part to its relatively poor spatial resolution, currently on the order of 3–6 mm (*3,4*). With this kind of spatial resolution, it is not possible to measure target density in small nodules and in many human and rodent brain regions relevant to disease etiology and pathophysiology.

Depth-encoding PET detector modules have been developed to mitigate parallax error (mispositioning of the line of response) for long scintillator crystals (*5*). This enables small diameter PET rings with reduced component cost per detector ring, large solid angle coverage for increased sensitivity, and reduced contribution of annihilation gamma ray acollinearity on spatial resolution when using crystals with small cross-sectional area (*4,6*). In addition, depth-of-interaction (DOI) information can be used to deconvolve optical photon transport in long crystals, thus improving timing resolution (*7,8*). Depth-encoding detectors based on dual-ended readout achieve the best continuous DOI resolution of < 2 mm (*9,10*). High resolution PET systems such as the mammography dedicated Clear-PEM have been developed using dual-ended DOI readout detectors (*11*), but these systems are too costly to be commercialized due to the large number of readout electronics compared to standard single-ended readout PET scanners. A recently developed high resolution variant of these detectors shows relatively poor energy and timing resolutions due to the use of glass light guides at the crystal-readout interface, which are required to achieve accurate crystal identification (*12*). Alternative single-ended readout detector modules have been proposed to obtain DOI information such as multi-layer phoswich blocks (*13,14*), retroreflectors for modules with monolithic scintillators (*15*), and other custom reflector designs (*16,17*). However, in all these designs tradeoffs exists among depth-encoding, cost, scintillator-to-readout coupling ratio, crystal identification accuracy, energy resolution, and timing resolution. To mitigate these tradeoffs, an ideal depth-encoding detector module is one with single-ended readout where the crystal array is directly coupled to silicon photomultiplier (SiPM) pixels, without any intermediate glass light guide, to minimize sharing of downward traveling scintillation photons across multiple pixels and retain good timing resolution. In addition, upward traveling photons, which do not contribute to the timing information, should be redirected via 180° bending of their paths towards the nearest neighboring SiPMs to retain good energy and DOI resolutions and mimic the behavior of dual-ended depth-encoding readout detectors.

Detector modules consisting of depolished multicrystal scintillator arrays coupled 4-to-1 to SiPM pixels on one side and a uniform glass light guide on the opposite side have recently been investigated in efforts to develop a practical and cost-effective high resolution time-of-flight (TOF) PET scanner, as well as achieve continuous DOI localization using single-ended readout (*8,18,19*). In these detector modules, energy weighted average method is utilized for crystal identification to achieve energy and DOI resolutions of 9% and 3 mm full width at half maximum (FWHM), respectively, using 1.53 x 1.53 x 15 mm^3 crystals and 3 × 3 mm^2 SiPM pixels (*8*). However, these arrays suffer from poor crystal identification along their edges and corners due to the lack of light sharing neighbors (*19*), an issue that must be addressed since the edge and corner pixels comprise 75% and 44% of 4×4 and 8×8 SiPM readout chips, respectively. Also, intercrystal light sharing is inefficient when using a uniform glass light guide since many upward traveling photons are reflected back into the primary column and the rest are isotropically shared with a Gaussian intensity distribution amongst neighbors. The problem with isotropic light sharing is the distribution of low-intensity signal across many SiPMs, the integrity of which will be severely affected by dark counts, resulting in degraded energy and DOI resolutions.

We introduce the concept of Prism-PET, a single-ended readout depth-encoding detector module which uses a specialized pattern of segmented prismatoid light guides (Figs. 1-2). Our Prism-PET detector modules have several key features. First, we utilize three distinct prismatoid designs (center, edge, and corner prismatoids) to mitigate edge and corner artifacts and thus achieve uniform crystal identification performance. Second, we confine intercrystal light sharing to only the nearest SiPM neighbors to create a deterministic and anisotropic intercrystal light sharing pattern and maximize signal-to-background ratio on those SiPMs to improve both energy and DOI resolutions. Note that the segmentation pattern is the key feature that improves crystal identification by decoupling adjacent crystals that would otherwise have similar readout patterns, thus the shape of each prismatoid is interchangeable (cuboids, pyramids, wedges, prisms, cupolae, frusta, etc.) In this study, right triangular prisms were used. Third, the right triangular prisms enhance intercrystal light sharing ratios, thus improving both crystal identification and DOI resolution. When optical photons enter the hypotenuse of the right triangular prisms they undergo 180° deviation, efficiently guiding them to neighboring crystals which are coupled to different readout pixels due to the offset crystal-to-prism coupling scheme with respect to crystal-to-pixel coupling (Figs. 1-2). Using experimental measurements, we demonstrate the advantages of our design in terms of crystal identification, energy resolution, and DOI resolution, including how Prism-PET enables up to 9-to-1 crystal-to-readout coupling, which can be used to substantially improve spatial resolution without increasing the number of readout channels (Figs. 2C-2D).

MATERIALS AND METHODS

Device Fabrication

We fabricated 3 different PET detector modules for comparison. One consisted of a 16 × 16 array of 1.4×1.4×20 mm^3 lutetium yttrium orthosilicate (LYSO) crystals coupled 4-to-1 on one side to an 8×8 SiPM readout array and on the opposite (radiation-receiving) side to a uniform glass light guide, similar to modules previously studied in the literature (*8,20*). The second module consisted of the same crystal and readout geometry, but we interchanged the single uniform glass light guide with a prismatoid light guide array which has unique design and layout of prisms at the corner, edge, and center of the detector module to optimize light sharing patterns (Figs. 2A-2B). The third module had the prismatoid light guide array and used the same SiPM array as the other modules but utilized a ~ 24 × 24 array of 0.96 × 0.96 × 20 mm^3 LYSO crystals to achieve 9-to-1 coupling (Figs. 2C-2D). In both Prism-PET modules, scintillator crystals are coupled to readout pixels and right triangular prisms in equal ratios. The coupling scheme of the prisms is offset from that of the readout pixels, such that each crystal is only coupled to other crystals belonging to different readout pixels (Fig. 2A). When optical photons enter the prismatoids following gamma ray interactions in the crystals, they are efficiently redirected to neighboring crystals due to the right triangular prism geometry, enhancing the light sharing ratio between pixels (Fig. 1). The geometry of each prismatoid is position dependent to decouple adjacent crystals along the edges and corners that would otherwise have similar readout patterns in order to optimize crystal separation.

Additionally, because the coupling scheme confines intercrystal light sharing to be between neighboring SiPMs that enhance crystal identification, one can match the index of refraction n between the scintillator columns, prisms, and coupling adhesive to further enhance light sharing and consequently improve DOI resolution and crystal identification. All prisms were fabricated using SF10 glass with n = 1.767 (instead of BK7 with n = 1.53, which is the material for the uniform glass light guide) and coupled to the scintillator arrays using NOA170 adhesive with n = 1.7. Barium sulfate ($BaSO_4$) is used as the reflector material between the crystals and prisms due to its high spatial performance that does not degrade energy or timing resolutions (*21*). SiPM saturation effects, which have been known to positively skew energy resolution and negatively impact DOI resolution, weren't accounted for in this study and will be explored in detail in future studies (*22*).

Detector Readout

The detector modules in this study consisted of LYSO crystal arrays fabricated at X-Lum (Shanghai, China) coupled (either 4-to-1 and 9-to-1) to 8 × 8 arrays of SiPMs (Hamamatsu S13361-3050AE-08). Data acquisition

was performed using TOFPET2 application-specific integrated circuits (ASICs) and a FEB/D v2 readout board from PETsys Electronics. Flood data was acquired on 4-to-1 and 9-to-1 coupled detector modules with prismatoid light guide arrays by uniformly exposing the modules with a 3 MBq Na-22 sodium point source (5 mm active diameter). 10,000,000 events from the 4-to-1 module and 22,500,000 events from the 9-to-1 module (to acquire an equal number of events per crystal) were used for flood histogram generation.

Electronic Tagging Setup

We experimentally measured the DOI performance of our modules on a per-crystal basis using a similar approach to the one described in Ref. (*18*). The modules were exposed to a Na-22 source at 5 different crystal depths (2, 6, 10, 14 and 18 mm) using lead collimation. The source was placed in a lead cylinder with a 1 mm pinhole. The pinhole was aligned with the DOI-aligned module on one side and a single 1.4×1.4×20 mm^3 crystal on a reference module on the other side. Coincidence events between the two modules were used to reject scatter events and only accept events along the intended line of response. The histograms for the DOI-estimation parameter (*18*), *w*, were calculated and plotted for all crystals. The *w* histograms were then converted to DOI space using linear regression to determine the slope between *w* and the ground truth DOI, which should be the center of each Gaussian peak. The widths of the Gaussian peaks converted to DOI space were used to calculate the DOI resolution of the crystals (Supplemental Fig. 1). DOI resolution is depth-dependent and equal to the FWHM of the Gaussian histograms. Overall crystal-specific DOI resolution was calculated as the average of the DOI resolutions across the measured depths (*18*). A typical center crystal from each module was used to calculate the DOI resolutions of each module.

RESULTS

We characterized the spatial performance of Prism-PET modules compared with the standard uniform glass light guide module using flood histograms of our fabricated modules (Fig. 3). The glass light guide module suffers from edge and corner effects, resulting in poor position-dependent crystal separation. Prism-PET enables excellent crystal separation throughout the entire detector array without edge and corner artifacts (Figs. 3A–3C), which has not previously been achieved in a 4-to-1 coupled detector module with single-ended TOF-DOI readout (*8,19,20*). We showed similar results with the 9-to-1 coupled Prism-PET module (Fig. 3C), demonstrating homogenous sub-millimeter crystal separation in a TOF-DOI PET detector module with 3.2 × 3.2 mm^2 SiPM pixels. Plotting 1D event positioning histograms (in the x-direction) confirms that Prism-PET has uniform crystal separation performance at the center, edges and corners (Fig. 4A). Prism-PET also achieves

14% and 16% energy resolution with DOI correction in the 4-to-1 and 9-to-1 coupled modules, respectively, whereas the uniform light guide only achieves 20% energy resolution (Fig. 4B).

We also experimentally measured the DOI performance for a single center crystal in each module (Fig. 5). The measured DOI resolution for the glass light guide was 5 mm FWHM, showing strong agreement with previously reported results (*19*). The Prism-PET modules achieved 2.5 mm FWHM DOI localization, the best resolution ever reported using single-ended readout. Increased depth-dependence of the *w* parameter is due to 1) controlled and deterministic light sharing pattern within the prismatoids, 2) increased light transfer from scintillators to light guides due to matched refractive indices, and 3) enhanced deviation of upward traveling optical photon path by 180° due to the right triangular prism geometry, all of which enhance light sharing between crystals coupled to the same prismatoid. DOI information can be used to improve both timing and energy resolution, the former by deconvolving depth-specific photon transport inside the scintillator and the latter by constructing depth-specific photopeaks (*8,18*). We achieved 9% and 10% energy resolution in the 4-to-1 and 9-to-1 coupled Prism-PET modules, respectively, and 13% energy resolution with the uniform light guide after applying DOI-based correction (Fig. 4B). Note that the DOI and energy resolution values will slightly change for better and worse, respectively, after implementing SiPM saturation correction (*22*); as a result, the values reported in this current study are more indicative of the relative performance of Prism-PET compared with the uniform light guide module rather than the absolute performance in practice.

DISCUSSION

We have developed a cost-effective and practical method for achieving high spatial and DOI resolution in multicrystal single-ended readout detector modules without introducing edge and corner artifacts. Our technology can be used to enable depth-encoding in clinical whole-body and total-body PET scanners (*23*) without increasing cost (prismatoid light guide array comprises less than 10% of the total cost of each Prism-PET module) and power consumption, while potentially improving spatial resolution (via 9-to-1 coupling of, for example, $2 \times 2 \times 20$ mm^3 crystals to 6×6 mm^2 readout pixels), sensitivity (via intercrystal Compton scatter recovery), and timing resolution (via DOI-correction of timing jitter). For small ring-diameter brain imaging, the 9-to-1 coupling ratio enables sub-millimeter spatial resolution, while extending axial field-of-view to about double that of whole-body PET scanners enables the same geometric sensitivity gain as the Explorer total-body PET scanner (Supplemental Fig. 2; Supplemental Note 1) (*8,23-26*). In addition, having 2.5 mm DOI resolution greatly mitigates parallax error and potentially enables achieving ~ 100 ps coincidence time

resolution via DOI-correction (*8*), which would enable even higher sensitivity and spatial resolution (*24-26*). These benefits yield a practical, cost-effective, and power efficient approach to achieving both high spatial resolution and high sensitivity at relatively low dose for quantitative *in vivo* functional and molecular imaging of many human body organs, including important structures of the brain that have not been resolvable with existing PET scanners such as the raphe nuclei, cholinergic basal forebrain nuclei, Locus coeruleus and hypothalamic nuclei, all of which are thought to play crucial roles in basic physiology as well as in the pathophysiology of common neurodegenerative and psychiatric disorders (*26*–*30*). The ability to visualize and quantitate these and similar targets has the potential to revolutionize molecular imaging in both the clinical and research arenas, providing hitherto unavailable tools for early diagnosis and basic research in oncology and brain disorders.

Another potential advantage of Prism-PET is the ability to more accurately identify the initial interaction site of Compton scatter events, further improving spatial resolution and sensitivity (Supplemental Note 2; Supplemental Figs. 3-4). Traditionally, Compton detection has been performed using multiple detector layers, but a recent paper outlined the criteria for localizing and decomposing Compton interactions using single-ended readout, citing high resolution DOI readout as a key feature for Compton scatter recovery (*31*). A uniform light guide is not optimal for this task because the SiPM pattern of individual events is random, whereas our Prism-PET modules create a deterministic light sharing pattern regardless of the interaction location inside the primary scintillator column (Fig. 1; Supplemental Fig. 4). Most notably, Prism-PET enables the decomposition of side-by-side scattered photon and recoil electron events, which are the most probable and most difficult to analyze scattering events, into their constituent energies, spatial location, and DOI (Supplemental Note 2). Compton scatter recovery is especially critical to retain high sensitivity in detector modules with small scintillator crystals since the scattered photon is more likely to be absorbed in a different crystal from the primary interaction site as crystal size decreases (*32*).

CONCLUSION

We have developed, fabricated and characterized our proposed Prism-PET detector module which is a true single-ended equivalent of a dual-ended depth-encoding readout using efficient 180° light bending reflectors for enhanced light sharing. We achieved 2.5 mm FWHM DOI resolution and up to 9-to-1 scintillator to SiPM coupling for high spatial resolution while directly coupling the crystal array to the SiPM pixels to minimize light leakage and retain high photon detection efficiency, which is required for good timing resolution. The top side reflector is comprised of an optimized pattern of segmented prismatoid light guides for efficient

redirection of scintillation photon paths from the primary crystal to selected nearest-neighboring SiPMs, thus mimicking very closely the operation of dual-ended readout detectors. This creates an anisotropic and deterministic pattern of signal that can be used to decompose a side-by-side Compton scattering events into their constituent energy and DOI information for the purpose of scatter recovery. Thus, we can expect to achieve high and uniform spatial resolution (9-to-1 coupling of ~ 1 mm crystals; absence of edge and corner artifacts due to enhanced light sharing; reduced spatial blur due to Compton-scattered photons via scatter recovery), high sensitivity (20-mm thick detectors, and intercrystal Compton scatter recovery), and good energy and timing resolutions (especially after applying DOI-correction) in compact systems (DOI encoding eliminates parallax error and permits smaller ring-diameter). With these unique combinations of features, cost-effective and compact TOF-DOI-Compton PET scanners could be developed based upon Prism-PET modules for small animal and human organ-specific functional and molecular imaging.

FINANCIAL DISCLOSURE

We gratefully acknowledge financial support from the National Institutes of Health (R21 EB024849).

DISCLAIMER

The authors declare no competing interests.

ACKNOWLEDGMENTS

We gratefully acknowledge help from PETsys Electronics, SA, Portugal.

KEY POINTS

QUESTION: Can we develop a high resolution (~ 1–2 mm crystals) single-ended readout (low-cost) PET detector module with simultaneous depth-encoding and time-of-flight capabilities? **PERTINENT FINDINGS:** We developed a segmented light guide made of an array of right triangular prisms that can be coupled to the radiation-receiving end of a PET module. Our light guide enables up to 9-to-1 scintillator-to-readout coupling (~ 1 mm spatial resolution when using standard 3.2 × 3.2 mm^2 readout pixels) and 2.5 mm

FWHM depth-of-interaction resolution (similar to the performance of dual-ended readout modules) without sacrificing sensitivity or coincidence time resolution. **IMPLICATIONS FOR PATIENT CARE:** Cost-effective high resolution and high sensitivity PET systems can be built with our detector module design, including preclinical, human organ-dedicated and total-body scanners.

REFERENCES

[1] Mankoff DA, Farwell MD, Clark AS, Pryma DA. Making molecular imaging a clinical tool for precision oncology: a review. *JAMA Oncol.* 2017;3:695–701.

[2] Slifstein M, Abi-Dargham A. Recent developments in molecular brain imaging of neuropsychiatric disorders. *Semin Nucl Med*. 2017;47:54–63.

[3] Van Sluis J, De Jong J, Schaar J, et al. Performance characteristics of the digital biograph vision PET/CT system. *J Nucl Med.* 2019;60:1031–1036.

[4] Moses WW. Fundamental limits of spatial resolution in PET. *Nucl Instr and Meth A*. 2011;648:S236–S240.

[5] Miyaoka RS, Lewellen TK, Yu H, McDaniel DL. Design of a depth of interaction (DOI) PET detector module. *IEEE Trans Nucl Sci.* 1998;45:1069-1073.

[6] Stickel JR, Cherry SR. High-resolution PET detector design: modelling components of intrinsic spatial resolution. *Phys Med Biol.* 2005;50:179–195.

[7] Seifert S, Schaart DR. Improving the time resolution of TOF-PET detectors by double-sided readout. *IEEE Trans Nucl Sci.* 2015;62:3–11.

[8] Pizzichemi M, Polesel A, Stringhini G, et al. On light sharing TOF-PET modules with 3 mm depth of interaction and 157 ps FWHM coincidence time resolution. *Phys Med Biol.* 2019;64:155008.

[9] Yang Y, Wu Y, Qi J, et al. A prototype PET scanner with DOI-encoding detectors. *J Nucl Med.* 2008;49:1132–40.

[10] Kuang Z, Wang X, Fu X, et al. Dual-ended readout small animal PET detector by using 0.5 mm pixelated LYSO crystal arrays and SiPMs. *Nucl Instr and Meth A.* 2019;917:1–8.

[11] Abreu MC, Aguiar JD, Almeida FG, et al. Design and evaluation of the clear-PEM scanner for positron emission mammography. *IEEE Trans Nucl Sci.* 2006;53:71–77.

[12] Du J, Yang Y, Bai X, et al. Characterization of large-area SiPM array for PET applications. *IEEE Trans Nucl Sci.* 2016;63:8–16.

[13] Schmand M, Eriksson L, Casey ME, et al. Performance results of a new DOI detector block for a high resolution PET-LSO research tomograph HRRT. *IEEE Trans Nucl Sci.* 1998;45:3000–3006.

[14] Seidel J, Vaquero JJ, Siegel S, et al. Depth identification accuracy of a three layer phoswich PET detector module. *IEEE Trans Nucl Sci.* 1999;46:485–490.

[15] Gonzalez-Montoro A, Aguilar A, Canizares G, et al. Performance study of a large monolithic LYSO PET detector with accurate photon DOI using retroreflector layers. *IEEE Trans Rad Plasma Med Sc.* 2017;1:229–237.

[16] Ito M, Lee MS, Lee JS. Continuous depth-of-interaction measurement in a single-layer pixelated crystal array using a single-ended readout. *Phys Med Biol.* 2013;58:1269–1282.

[17] Kuang Z, Yang Q, Wang X, et al. A depth-encoding PET detector that uses light sharing and single-ended readout with silicon photomultipliers. *Phys Med Biol.* 2018;63:045009.

[18] Pizzichemi M, Stringhini G, Niknejad T, et al. A new method for depth of interaction determination in PET detectors. *Phys Med Biol.* 2016;61:4679–4698.

[19] Niknejad T, Pizzichemi M, Stringhini G, et al. Development of high-resolution detector module with depth of interaction identification for positron emission tomography. *Nucl Instr and Meth A*. 2017;845:684–688.

[20] Stringhini G, Pizzichemi M, Ghezzi A, et al. Development of a high resolution module for PET scanners. *J Instrum.* 2017;12:C02073–C02073.

[21] Kuang Z, Wang X, Li C, et al. Performance of a high-resolution depth encoding PET detector using barium sulfate reflector. *Phys Med Biol.* 2017;62:5945–5958.

[22] Otte AN, Barral J, Dolgoshein B, et al. A test of silicon photomultipliers as readout for PET. *Nucl Instr and Meth A*. 2005;545:705-715.

[23] Badawi RD, Shi H, Hu P, et al. First human imaging studies with the explorer total-body PET scanner. *J Nucl Med.* 2019;60:299–303.

[24] Surti S. Update on time-of-flight PET imaging. *J Nucl Med.* 2015;56:98-105.

[25] Reddin JS, Scheuermann JS, Bharkhada D, et al. Performance evaluation of the SiPM-based Siemens Biograph Vision PET/CT system. In: *Conference Record of the 2018 IEEE Nuclear Science Symposium and Medical Imaging Conference*. Sydney, AU: IEEE; 2018.

[26] Gong K, Majewski S, Kinahan PE, et al. Designing a compact high performance brain PET scanner—simulation study. *Phys Med Biol.* 2016;61:3681-3697.

[27] Hornung JP. The human raphe nuclei and the serotonergic system. *J Chem. Neuroanat.* 2003;26:331–343.

[28] Mufson EJ, Ginsberg SD, Ikonomovic MD, DeKosky ST. Human cholinergic basal forebrain: Chemoanatomy and neurologic dysfunction. *J Chem Neuroanat*. 2003;26:233–242.

[29] Betts MJ, Kirilina E, Otaduy MCG, et al. Locus coeruleus imaging as a biomarker for noradrenergic dysfunction in neurodegenerative diseases. *Brain*. 2019;142:2558–2571.

[30] Barbosa DA, de Oliveira-Souza R, Santo FM, et al. The hypothalamus at the crossroads of psychopathology and neurosurgery. *Neurosurg Focus*. 2017;43:1–11.

[31] Makek M, Bosnar D, Pavelić L. Scintillator pixel detectors for measurement of Compton scattering. *Condens Matter*. 2019;4:24.

[32] Hsu DF, Freese DL, Innes DR, Levin CS. Intercrystal scatter studies for a 1 mm^3 resolution clinical PET system prototype. *Phys Med Biol.* 2019;64:095024.

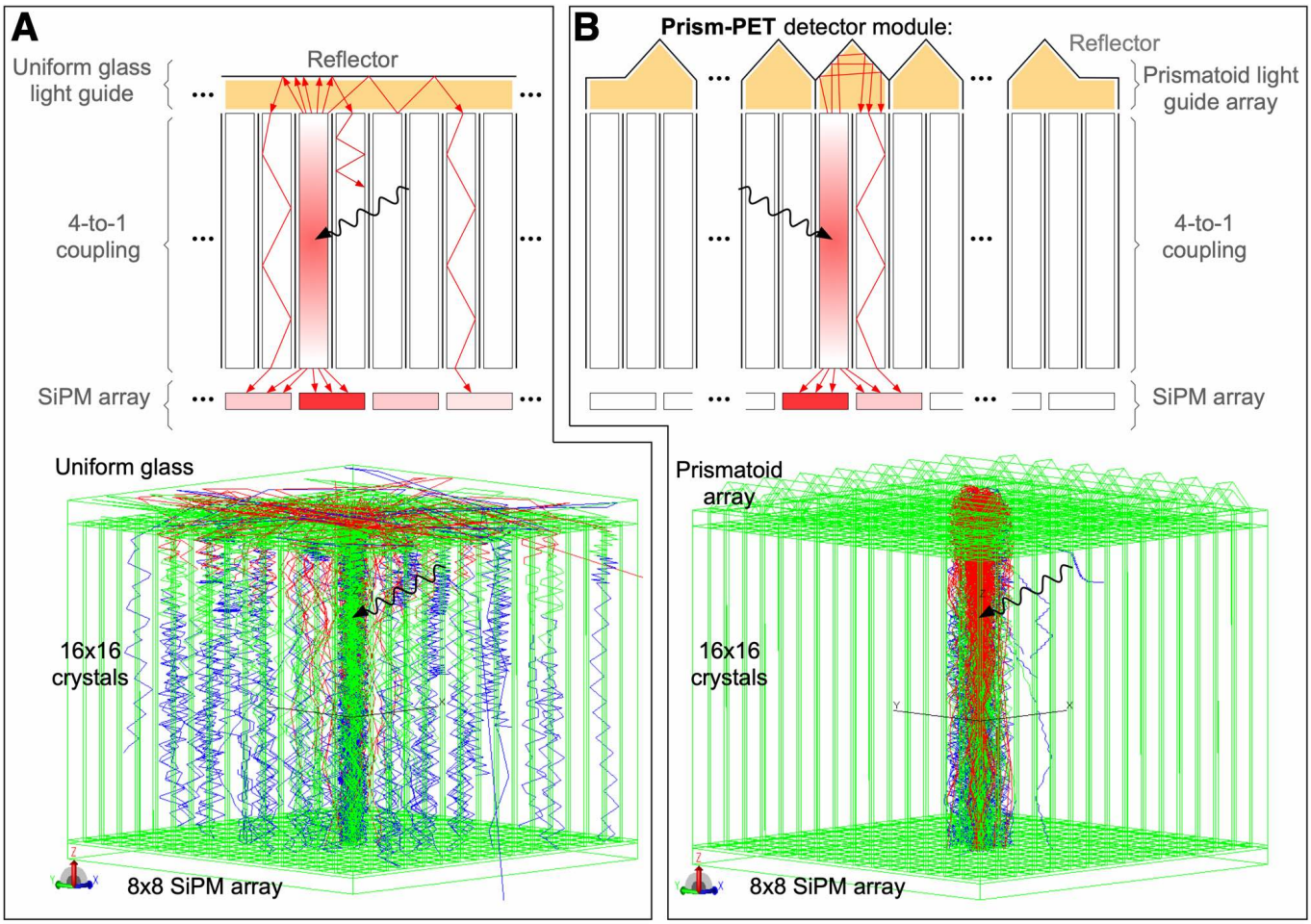

Figure 1. Comparison of light sharing scheme between (A) the uniform glass light guide module and (B) Prism-PET as simulated in TracePro. Light is uniformly distributed via light sharing in the uniform light guide, while the prismatoid light guide array in Prism-PET confines light sharing to crystals coupled to the same prismatoid and enhances intercrystal light sharing ratios.

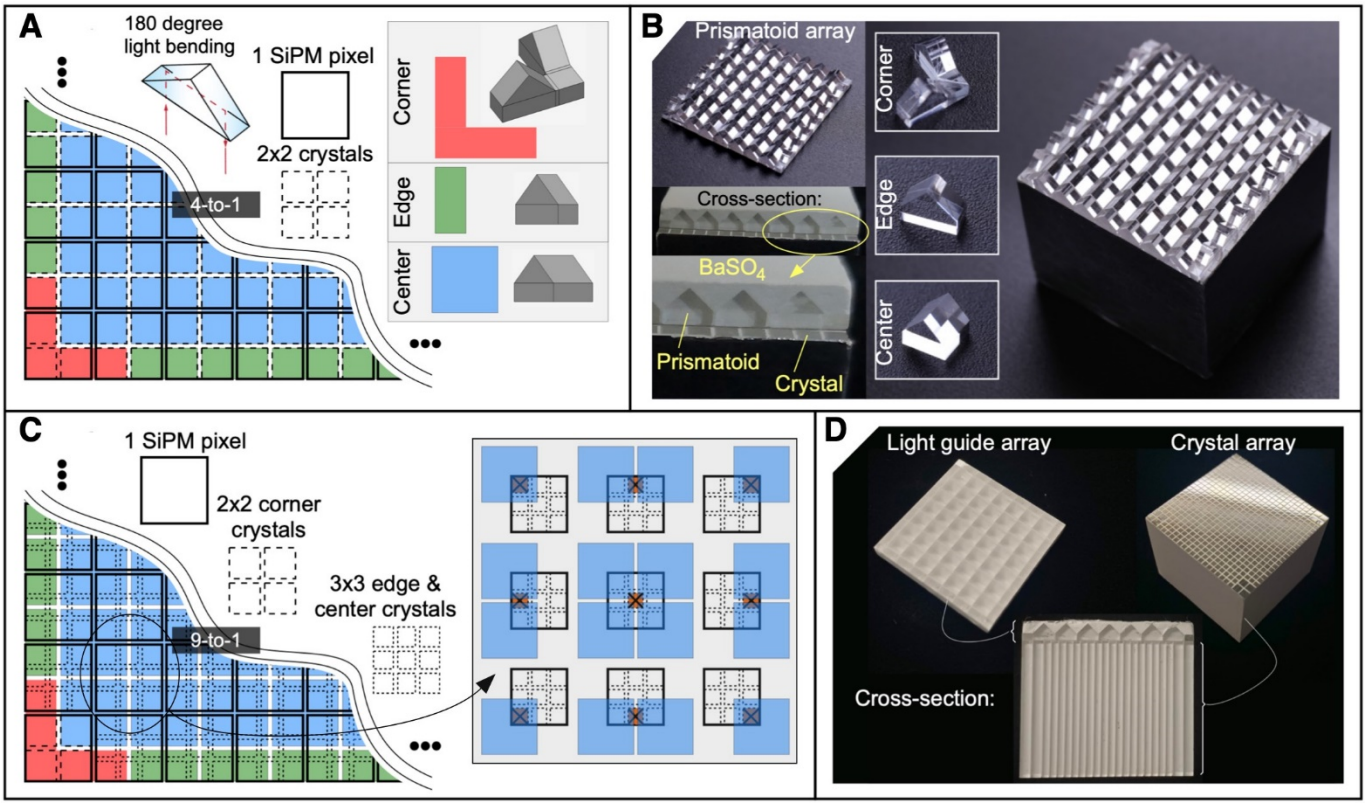

FIGURE 2. Concepts and fabrication of Prism-PET detector modules. (A),(B) Schematic diagram and fabrication of a 4-to-1 coupled Prism-PET module. (C),(D) Schematic diagram and fabrication of a 9-to-1 coupled Prism-PET module. Inset in (C) shows the unique readout pattern of each crystal belonging to a single prismatoid light guide in the 9-to-1 coupled module.

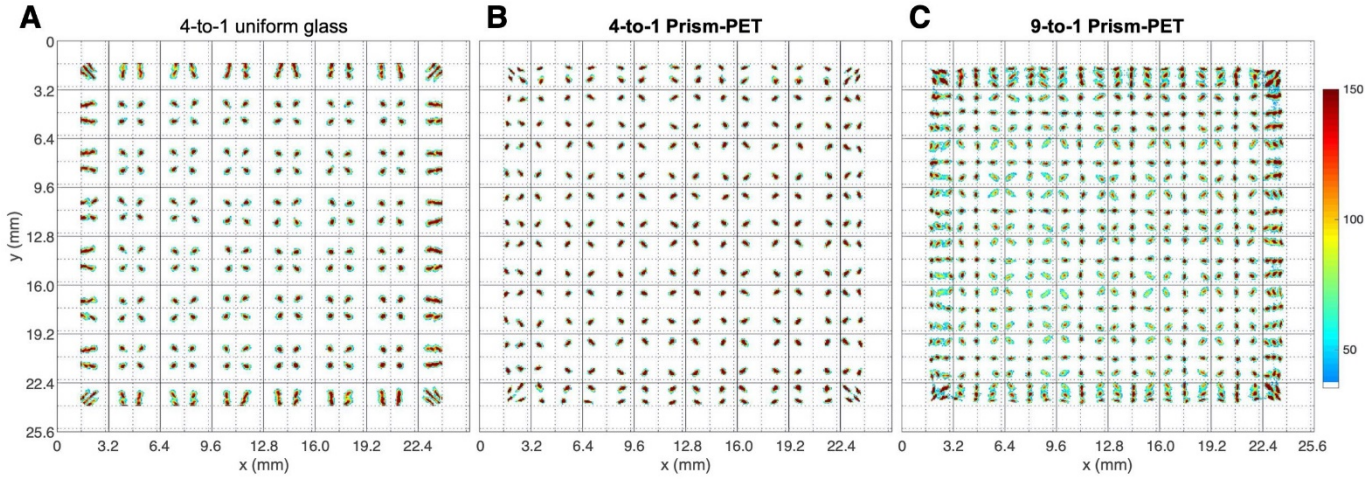

FIGURE 3. Experimental results for crystal identification. Flood histogram data for (A) the 4-to-1 coupled module with a flat uniform glass light guide (B) the 4-to-1 coupled Prism-PET module, and (C) the 9-to-1 coupled Prism-PET module.

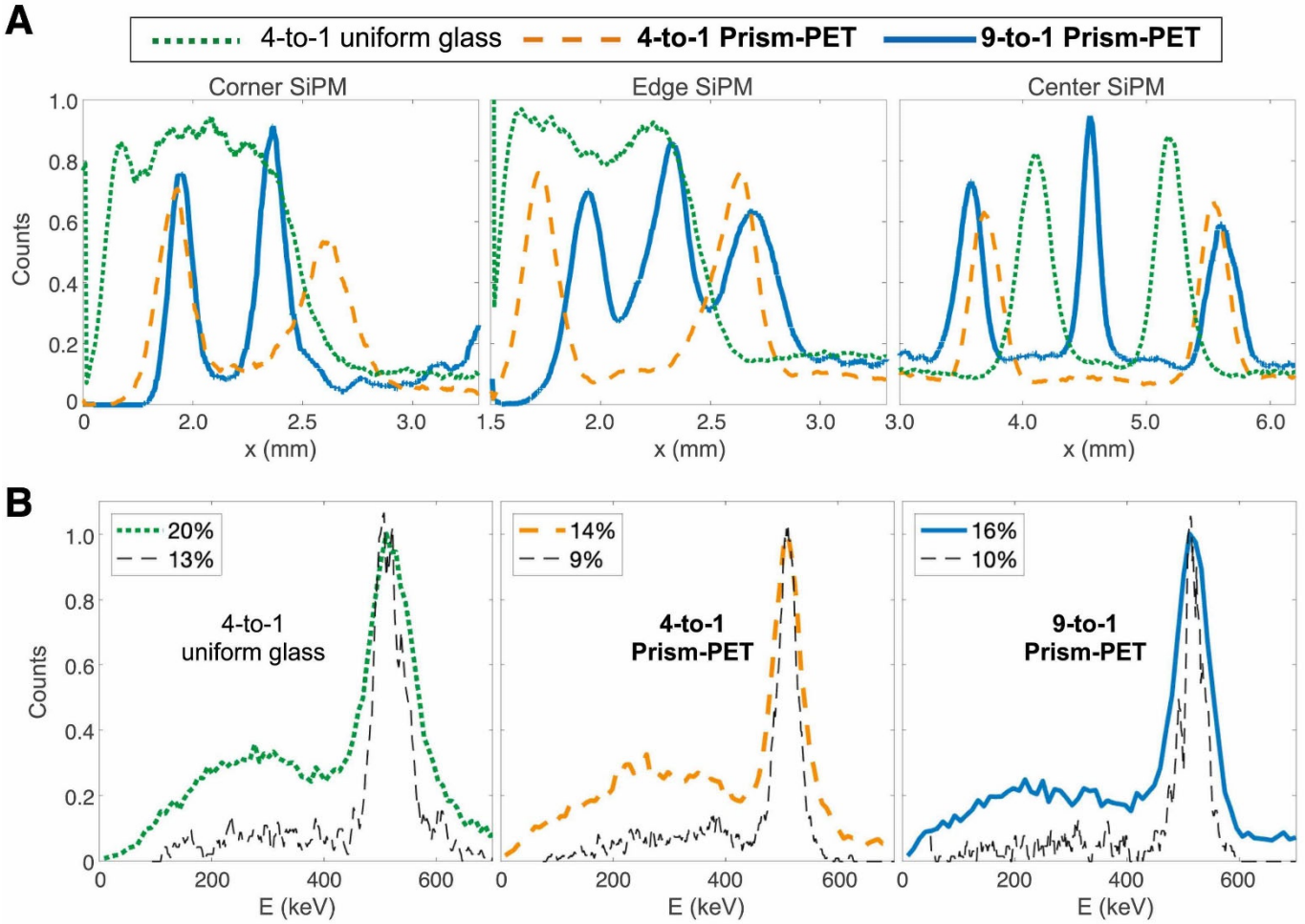

FIGURE 4. (A) 1D Gaussian histograms showing crystal separation in the x-direction from a corner, edge and center readout pixel for all 3 modules. (B) Filtered energy spectrums with (black) and without (colored) DOI-correction from a center crystal in all 3 modules.

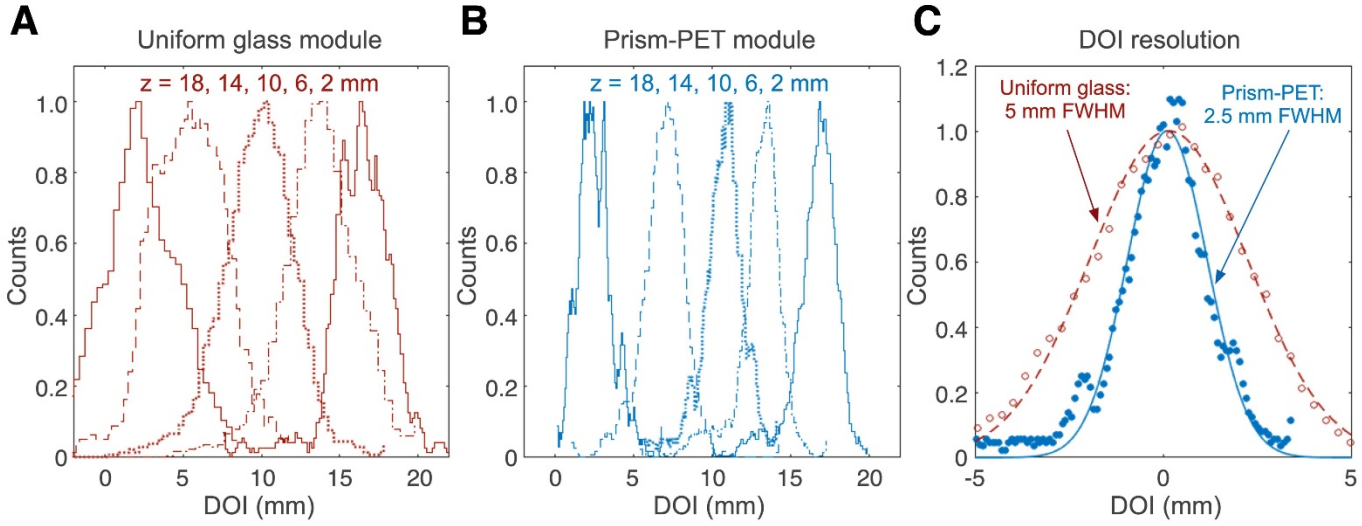

FIGURE 5. Experimental results for DOI resolution. DOI-specific histograms of calculated interaction depths in a center crystal of 4-to-1 coupled detector modules with (A) uniform glass and (B) prismatoid light guides. (C) Comparison of DOI resolution based on the light guide used. The Prism-PET detector module achieves a two-fold improvement in DOI resolution over the uniform glass light guide.

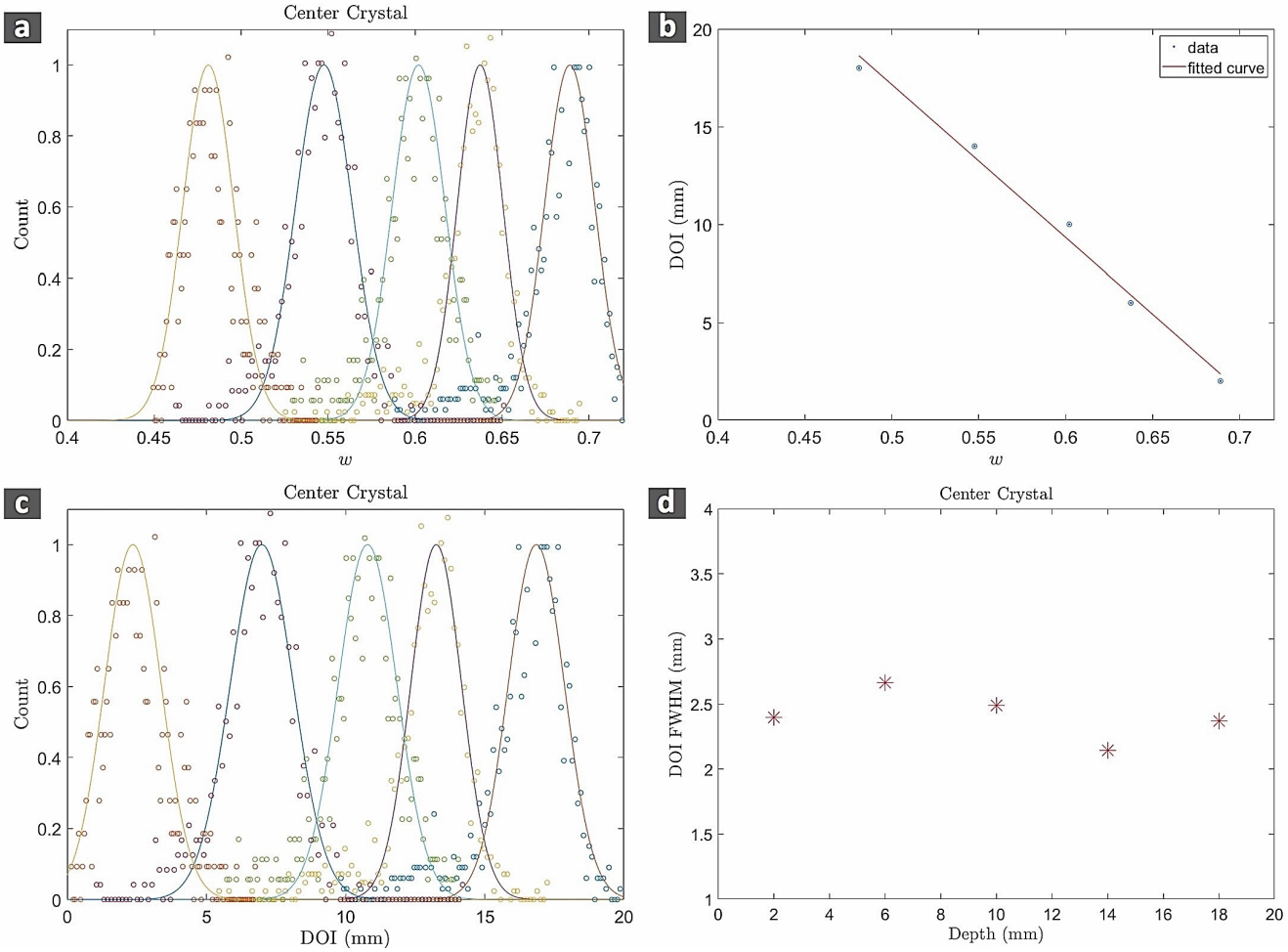

SUPPLEMENTAL FIGURE 1. Conversion from DOI-specific *w* histograms to DOI histograms showing the DOI resolution of a single crystal at each depth. (A) Histograms of the DOI-estimation parameter *w* acquired at 2, 6, 10, 14 and 18 mm. (B) Fit between *w* and DOI via linear regression. (C) DOI histograms generated by taking the *w* histograms in (A) and multiplying by the slope of the linear fit in (B). (D) DOI resolution at each acquired depth based on the width of the Gaussians in (C).

Supplemental Note 1. Sensitivity

Perhaps the most important parameter to consider when building a PET system is gamma ray detection sensitivity, which is directly related to signal-to-noise ratio (SNR) and thus determines patient throughput, delivered dose and image quality. Monte Carlo simulations using highly advanced software such as GATE are the most reliable way to model and calculate system-level sensitivity. However, relative improvements in sensitivity and comparisons between systems can be done analytically by calculating (a) geometric sensitivity and (b) sensitivity gain based on coincidence time resolution (CTR) for time-of-flight readout (TOF), which is equal to the SNR gain squared (*1*)

$$\Delta(SNR) = \sqrt{\frac{D}{\Delta x}}$$
$$\Delta(Sens) = \Delta(SNR)^2 = \frac{D}{\Delta x} \quad (1)$$

where D is the diameter of the object being imaged and Δx is the length of the reconstructed line segment along the line-of-response, which is directly proportional to the CTR (Δt):

$$\Delta x = \frac{c * \Delta t}{2} \tag{2}$$

An example of a dedicated brain PET scanner that can be built with Prism-PET detector modules would be a cylindrical ring with 50 cm axial length and 25 cm diameter. Supplemental Fig. 2A shows the proposed brain Prism-PET scanner dimensions compared to those of an example whole-body (Siemens Biograph Visions) and total-body (Explorer) PET scanner. Having a small ring diameter and large axial field-of-view greatly improves the geometric efficiency (Supplemental Fig. 2B) at the cost of greatly increased parallax error and partial volume effect, which can be mitigated by performing depth-of-interaction (DOI) readout (*2*). As a result, small diameter organ-specific scanners should only be built with detector modules with DOI localization capabilities, such as our Prism-PET modules.

A recent paper demonstrated that DOI readout can also be used to recover CTR for TOF readout by deconvolving the DOI-dependence on coincidence timing (i.e., differences in path length in optical photons) (*3*). Assuming we have the same CTR reported in this paper (~ 150 ps), which is a safe lower bound estimate since our modules have better DOI resolution (2.5 mm vs. 3 mm), Prism-PET enables a TOF sensitivity gain close to a factor of 10 based on Eq. 1 when imaging an object with $D \sim 20$ cm such as the human brain (Supplemental Fig. 2C). The TOF sensitivity gain for human brain imaging is slightly lower for Siemens Biograph Vision, which achieves ~ 220 ps CTR (*4*), and much lower for the Explorer (Supplemental Fig. 2C), which has CTR > 400 ps (*5*).

Supplemental Fig. 2D shows the overall effective sensitivity gain for human brain imaging when taking both geometric efficiency and TOF sensitivity gain into account. Based on our calculations, our proposed Prism-PET scanner may enable a three-fold and four-fold improvement in sensitivity compared to the Siemens Biograph Vision and Explorer scanners, respectively. However, experimental results are required to confirm Prism-PET's higher sensitivity via enhanced DOI-corrected CTR compared to the other state-of-the-art PET scanners.

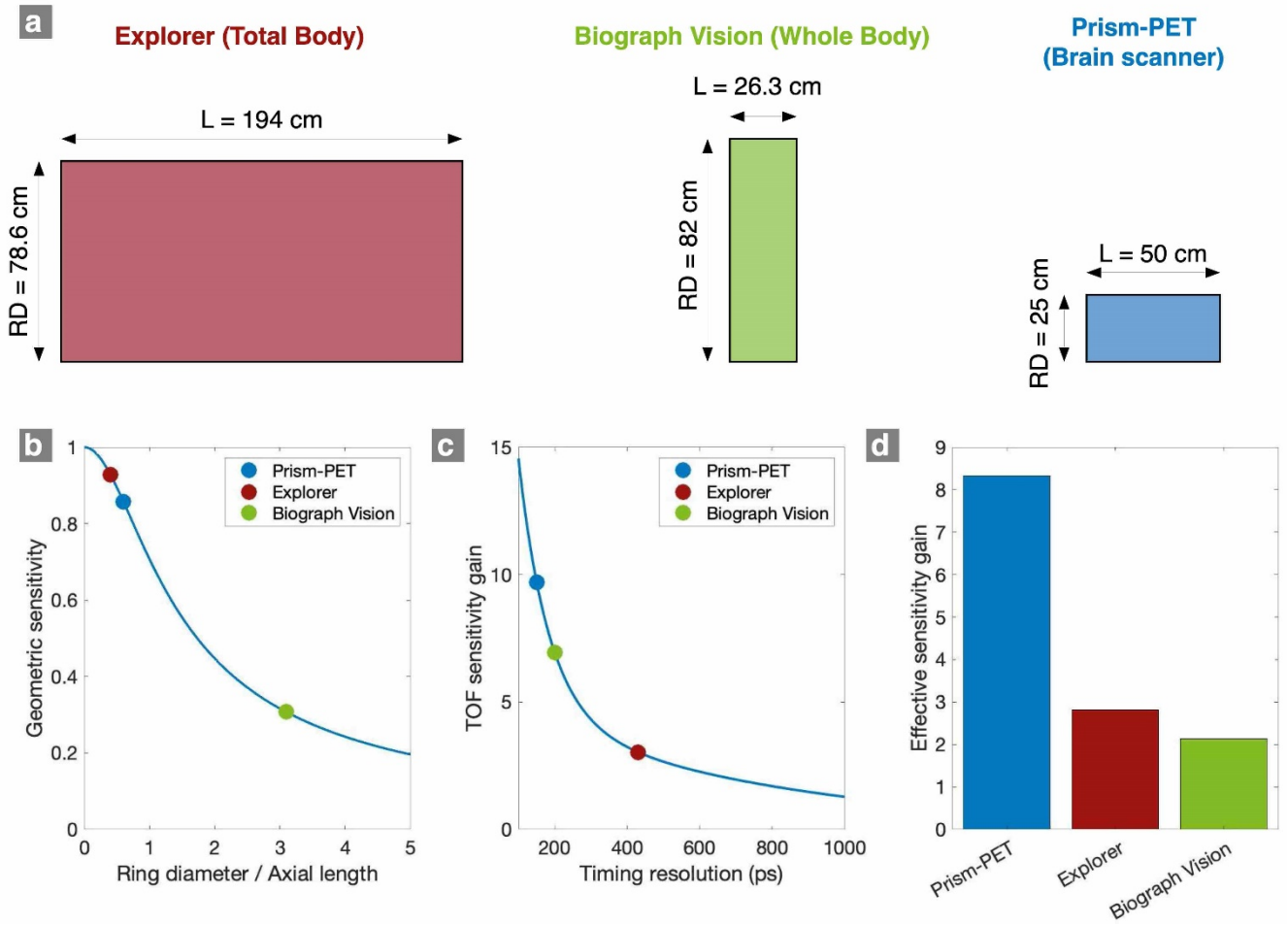

SUPPLEMENTAL FIGURE 2. (A) Dimensions and geometric coverage of the Siemens Biograph Vision, Explorer Total-Body PET scanner, and an example of a Prism-PET brain scanner. (B) Geometric sensitivity for a point source positioned in the center of each of the scanners shown in (A). (C) Relative sensitivity gain as a function of coincidence timing resolution. (D) Effective sensitivity gain calculated as the product between geometric efficiency (as shown in (B)) and TOF sensitivity gain (as shown in (C)).

Supplemental Note 2. Compton Localization

Prism-PET enables Compton scatter energy decomposition (and thus localization) due to its deterministic light sharing pattern. Let's assume we have a 16 × 16 array of lutetium yttrium orthosilicate (LYSO) crystals with a Prism-PET light guide coupled 4-to-1 to an 8 × 8 array of silicon photomultiplier (SiPM) pixels. We can approximate that each 511 keV gamma rays will produce a signal on 4 different pixels due to light sharing. The light sharing ratios between all crystals belonging to the same prismatoid can be measured directly using photoelectric events from flood data. Using this information, we can decompose the energies of the primary interaction (i.e., recoil electron) and secondary interaction site (i.e., scattered gamma ray). Once we have the decomposed energies, we can localize the two independently absorbed events in the scintillation blocks and determine the scattering angles and DOI. For the Prism-PET module, identifying a side-by-side Compton scattering event is possible because of the change from random light sharing for photoelectric events to a deterministic pattern (Figs. 4 and 5).

Classical Compton energy decomposition can be performed as follows. The total absorbed energies E_A and E_B by the constituent elements A and B (scatter and recoil electron) are given as the summation of the energies in all 4 SiPMs

$$E_{\mathrm{A}} = \sum_{i=1}^{4} E_{\mathrm{A}i}$$
$$E_{\mathrm{B}} = \sum_{i=1}^{4} E_{\mathrm{B}i} \tag{3}$$

where E_{A1} and E_{B1} are the maximum deposited energies in the SiPM coupled to the interacted crystal pixels and $E_{A2,3,4}$ and $E_{B2,3,4}$ are the deposited energies in the neighboring columns due to light leak at the bottom (from the SiPM side) and at the top via the prism-mirror light guide. The experimental results in Supplemental Fig. 3A illustrates the four known parameters E_{1-4} corresponding to the detected energies by each of the four pixels after the side-by-side Compton scattering event, where the total gamma particle energy deposited is

$$E_\gamma = \sum_{i=1}^{4} E_i = E_{\mathrm{A}} + E_{\mathrm{B}} \tag{4}$$

Note that the energies of the constituent elements of the Compton scattering event, namely E_{A1-4} and E_{B1-4}, are unknown. Writing the equations based on the measured energies we obtain

$$E_1 = E_{A1} + E_{B4}$$
$$E_2 = E_{A2} + E_{B1}$$
$$E_3 = E_{A3} + E_{B2}$$
$$E_4 = E_{A4} + E_{B3} \tag{5}$$

where we have 4 equations and 8 unknowns. However, the deposited energies in the neighboring columns are correlated. Let's consider the inset plot in Supplemental Fig. 3B where the maximum deposited energy occurred in the top-left SiPM. Given that the sharing fraction with the 3 neighbors depends on their proximity to the interacted crystal, and using the Pythagorean theorem by forming a right triangle using centers of the 3 neighbors as its vertices, we arrive at

$$\epsilon_{24} = d_{12}/d_{14} = 1 \xrightarrow{\text{thus}} E_{\mathrm{A}4} = \epsilon_{24} E_{\mathrm{A}2} = E_{\mathrm{A}2}$$
$$\epsilon_{23} = d_{12}/d_{13} = 1/\sqrt{} \qquad\qquad _{\mathrm{A}2} \tag{6}$$

where, for example, d_{12} is the distance between the centers of the primary SiPM 1 and neighboring SiPM 2. Substituting Eq. 6 in Eq. 5 we get

$$E_1 = E_{A1} + E_{B2}$$

$$E_2 = E_{A2} + E_{B1}$$

$$E_3 = 0.7E_{A2} + E_{B2}$$

$$E_4 = E_{A2} + 0.7E_{B2} \quad (7)$$

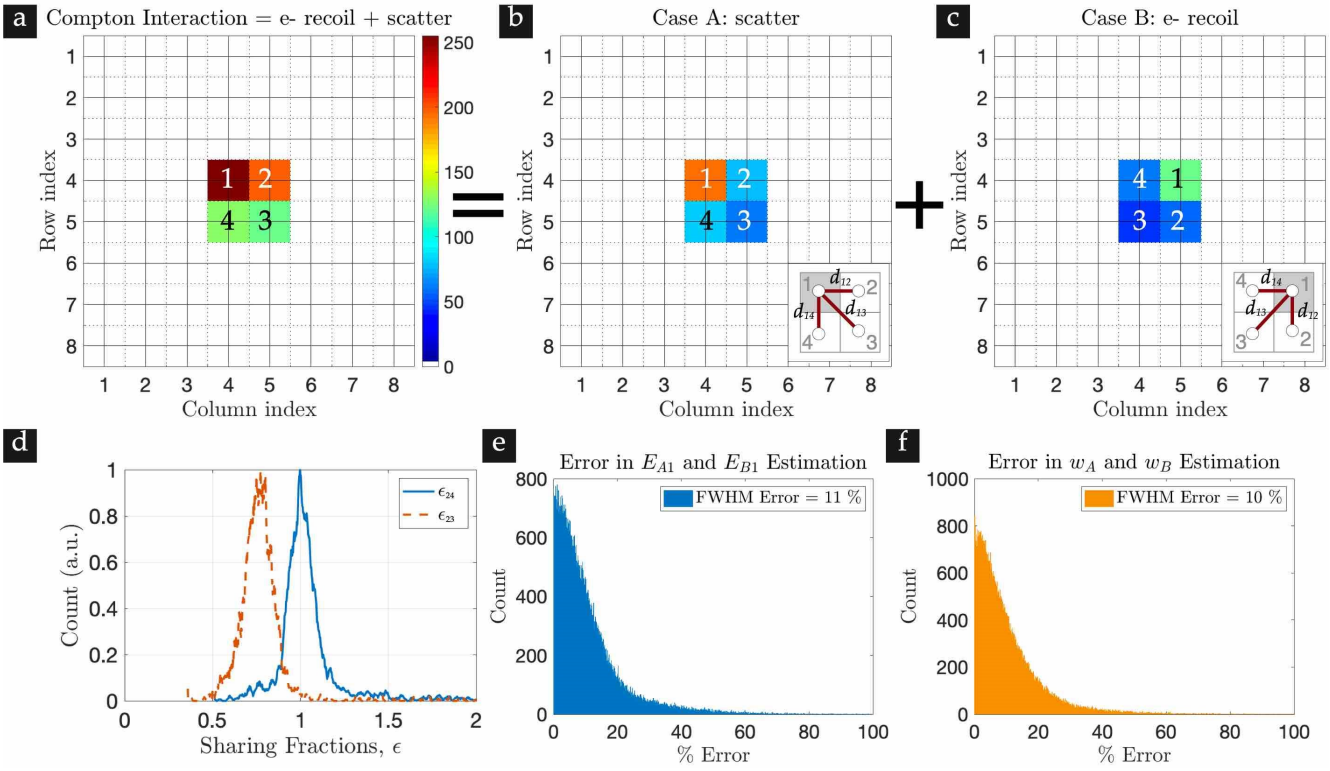

SUPPLEMENTAL FIGURE 3. (A)-(C) Example of Compton energy decomposition in a multicrystal scintillator array with Prism-PET. (D) Examples of light sharing fraction ratios between pixel 1 and neighboring pixels (as labeled in (A)-(C)). In one case (blue), both pixels (2 and 4) are adjacent to pixel 1 resulting in equal light sharing fractions, while in the other case (orange) pixel 3 is diagonally across from pixel 1 resulting in a smaller light sharing fraction. (E),(F) Energy and DOI error of Compton interaction decomposition for Prism-PET.

where we now have 4 equations and 4 unknowns. Note that in practice the sharing fractions will have spatial variations from the ideal cases shown in Eq. 6 due to some small and unavoidable misalignments between the prism-mirror light guides and the scintillator columns. However, as shown in Supplemental Fig. 3D, they can be obtained empirically across the array by analyzing the sharing fractions from individual photoelectric events obtained using the flood-histogram experiment. Supplemental Figs. 4B-C depict the two decomposed elements of a measured side-by-side Compton scattering event based on the above analysis.

Given that our modules have DOI localization, we can represent the DOI variables as

$$w_A = E_{A1}/E_A$$

$$w_B = E_{B1}/E_B \quad (8)$$

As shown in Supplemental Figs. 4E-F, the percent error for our estimation of $\{E_{A1},E_{B1}\}$ and $\{w_A,w_B\}$ based on 200,000 experimental Gamma events is ~ 10%. The error can be further reduced using convolutional neural networks as the estimator specially since we can collect millions of Gamma events as training dataset using the flood-histogram experiment.

An example of how a Compton event where the recoil electron and scattered γ-ray are fully absorbed in adjacent scintillators in two different SiPMs can be decomposed into its constituent elements can be seen in Supplemental Fig. 3. Calculating the DOI variable w using classical Compton decomposition resulted in 11% full width at half maximum (FWHM) error (Supplemental Fig. 3E). In addition, Compton decomposition results in 15% FWHM energy error (Supplemental Fig. 3F).

Experimental results showing several examples of Compton events absorbed in adjacent crystals in a Prism-PET module vs. a module with a flat glass light guide can be seen in Supplemental Fig. 4. The light sharing pattern in the glass light guide module is random, making it difficult (and in most cases, impossible) to decompose the detected energies into the constituent energies of the scattered photon and recoil electron. Due to the right triangular prism geometry, the light sharing pattern is deterministic in the Prism-PET module, making it practical to decompose the event into its constituent energies based on the known light sharing ratios between crystals.

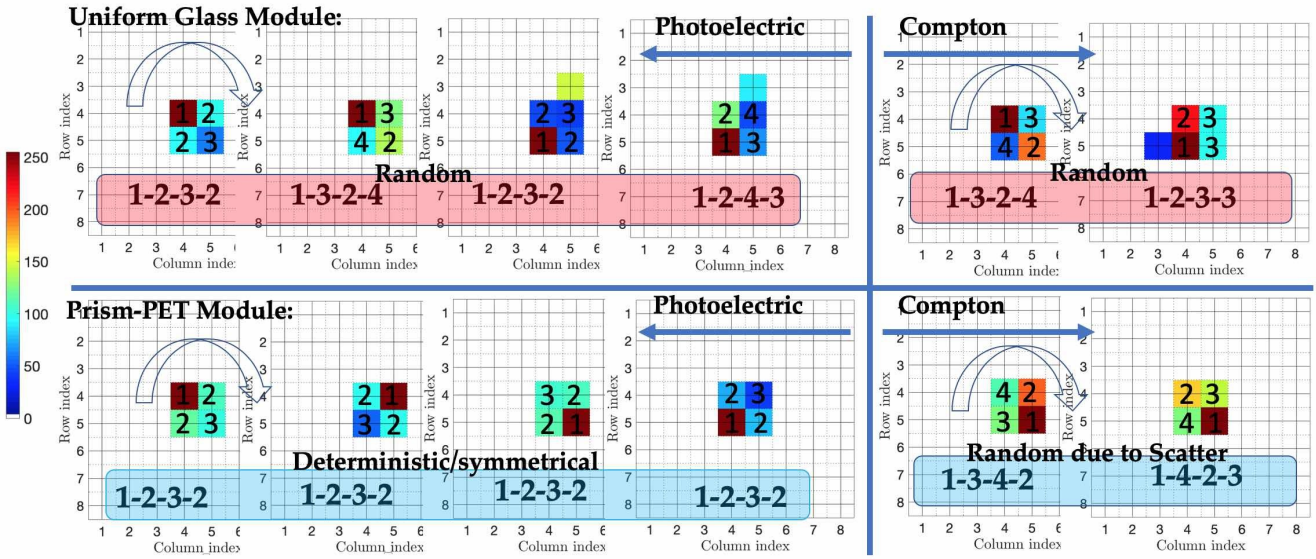

SUPPLEMENTAL FIGURE 4. Random light sharing pattern of a glass light guide (top) vs. deterministic light sharing pattern of Prism-PET (bottom).

References

[1] Surti S. Update on time-of-flight PET imaging. *J Nucl Med.* 2015;56:98–105.

[2] Gong K, Majewski S, Kinahan PE, et al. Designing a compact high performance brain PET scanner—simulation study. *Phys Med Biol.* 2016;61:3681–3697.

[3] Pizzichemi M, Polesel A, Stringhini G, et al. On light sharing TOF-PET modules with 3 mm depth of interaction and 157 ps FWHM Coincidence Time Resolution. *Phys Med Biol.* 2019;64:155008.

[4] Reddin JS, Scheuermann JS, Bharkhada D, et al. Performance Evaluation of the SiPM-based Siemens Biograph Vision PET/CT System. In: *Conference Record of the 2018 IEEE Nuclear Science Symposium and Medical Imaging Conference.* Sydney, AU: IEEE; 2018.

[5] Badawi RD, Shi H, Hu P, et al. First human imaging studies with the explorer total-body PET scanner. *J Nucl Med.* 2019;60:299–303.